Driving magma to the surface: The 2011–2012 El Hierro Volcanic Eruption

Carmen López[1] [iD], Maria A. Benito-Saz[1] [iD], Joan Martí[2] [iD], Carmen del-Fresno[1] [iD], Laura García-Cañada[1] [iD], Helena Albert[3] [iD], and Héctor Lamolda[1,4] [iD]

[1]Observatorio Geofísico Central, Instituto Geográfico Nacional, Madrid, Spain, [2]Group of Volcanology, SIMGEO, Institute of Earth Sciences JaumeAlmera, Barcelona, Spain, [3]Earth Observatory of Singapore, Nanyang Technological University, Singapore, Singapore, [4]Universidad Politécnica de Madrid, Madrid, Spain

Abstract We reanalyzed the seismic and deformation data corresponding to the preeruptive unrest on El Hierro (Canary Islands) in 2011. We considered new information about the internal structure of the island. We updated the seismic catalog to estimate the full evolution of the released seismic energy and demonstrate the importance of nonlocated earthquakes. Using seismic data and GPS displacements, we characterized the shear-tensile type of the predominant fracturing and modeled the strain and stress fields for different time periods. This enabled us to identify a prolonged first phase characterized by hydraulic tensile fracturing, which we interpret as being related to the emplacement of new magma below the volcanic edifice on El Hierro. This was followed by postinjection unidirectional migration, probably controlled by the stress field and the distribution of the structural discontinuities. We identified the effects of energetic magmatic pulses occurring a few days before the eruption that induced shear seismicity on preexisting faults within the volcano and raised the Coulomb stress over the whole crust. We suggest that these magmatic pulses reflect the crossing of the Moho discontinuity, as well as changes in the path geometry of the dyke migration toward the surface. The final phase involved magma ascent through a prefractured crust.

1. Introduction

The occurrence of seismic swarms, surface deformation, and thermal and geochemical anomalies constitute the main evidence for the reactivation of a volcanic system [e.g., *Phillipson et al.*, 2013], and the study of their spatial and temporal variations constitute the most robust tool for forecasting the future behavior of volcanic unrest [*Sparks*, 2003].

During the final stages of preeruptive volcanic unrest, certain geophysical and geodetical features are usually observed: an overall acceleration in seismicity and ground deformation [e.g., *Bell and Kilburn*, 2011], shallower seismicity [e.g., *Battaglia et al.*, 2005], seismic migration [e.g., *Caudron et al.*, 2015], and an apparent lack of activity (hours to minutes) before the reinforcement or the onset of the eruption [e.g., *Roman and Heron*, 2016]. Several well-documented eruptions show some, if not all, of these precursory features [e.g., *Vinciguerra*, 2002; *Battaglia et al.*, 2005; *Bell and Kilburn*, 2011; *López et al.*, 2012; *Sigmundsson et al.*, 2015; *Caudron et al.*, 2015], which suggests that similar fundamental processes may occur within these volcanoes. Whether this reactivation gives rise to an eruption or only represents a departure from the normal state of activity of the volcano will depend on the type of processes that have caused the reactivation (e.g., magmatic, hydrothermal, and/or tectonic). However, the processes preceding a new eruption are complex and poorly known, and there are still many unanswered questions regarding the requirements for an irreversible failure of the Earth's crust and nonstop magma migration from deeper levels to the surface. It is also difficult to interpret the precursory signals recorded by monitoring networks and to understand the nature and extent of the physical processes that cause them. Some of the difficulties arise from the incompleteness of monitoring data and the lack of previous knowledge of the volcanic systems (e.g., type of magma, internal structure, local and regional stresses). Instrumental monitoring data about unrest preceding monogenetic eruptions is still limited and the available information is mainly based on historical records [*Albert et al.*, 2016].

The observational data collected during the volcanic eruption on El Hierro in 2011–2012 provides an opportunity to address this topic. During the unrest (19 July to 10 October 2011), the Instituto Geográfico

Nacional's (IGN, Spain) monitoring network recorded intense seismicity and surface deformation, thereby suggesting magma accumulation and migration near the base of the crust below the island [see *López et al.*, 2012]. Despite all the scientific work devoted to this eruption [e.g., *López et al.*, 2012, 2014; *Martí et al.*, 2013, 2017; *Tárraga et al.*, 2014; *González et al.*, 2013; *Klügel et al.*, 2015; *Sainz-Maza* et al., 2014; *García-Yeguas et al.*, 2014; *Meletlidis et al.*, 2015; *Telesca et al.*, 2014, 2015; *Díaz-Moreno et al.*, 2015], there are still a number of unresolved questions regarding the unrest process. Did the seismicity truly define the path followed by the magma during the preeruptive unrest process? When was the new magma emplaced below the island? Which processes controlled the aseismic upward migration of the magma to the surface and why was it aseismic?

Magma migration through the brittle part of the lithosphere causes fracturing and dike propagation, which is driven by magma overpressure, the physical properties of the magma and crust, and the local and regional stress fields [e.g., *Pinel and Jaupart*, 2004; *Maccaferri et al.*, 2011]. In light of new published information about the internal structure below El Hierro [*García-Yeguas et al.*, 2014; *Martí et al.*, 2017], we reanalyzed the seismic and geodetic data recorded during El Hierro volcanic unrest to gain deeper understanding of the nature of the precursory signals and how to correctly interpret them when only limited data are available. We applied methods for retrieving the maximum amount of information from the data and were able to obtain new details regarding the eruptive mechanism. The results will not only be useful for understanding the eruption on El Hierro and its unrest process but also for comprehending the dynamics of other volcanoes in active monogenetic fields.

1.1. El Hierro Overview

El Hierro is the smallest and youngest of the group of seven volcanic islands that form the Canarian Archipelago located off the northwest coast of Africa [*Carracedo et al.*, 2002] (Figure 1a). In July 2011, after more than 200 years of quiescence, a period of volcanic unrest began that culminated in a submarine eruption on 10 October 2011, less than 2 km off the island's southern coast. The eruption lasted for 4 months and generated serious bubbling and the emission of ash and scoriaceous fragments onto the surface of the sea [e.g., *Meletlidis et al.*, 2015].

Structural studies carried out on El Hierro before the eruption revealed clear lithospheric anomalies below the island. A 3-D-lithospheric gravimetric inversion over a wide area around the Canary Islands found a regional N-S oriented Bouguer gradient associated with a wavelength of 40 km (corresponding to a depth of 48–128 km) passing through El Hierro Island and to the west of the island of La Palma (Figure 1b). In addition, two shallow gravity minima were identified to the NE and SW of El Hierro, with Bouguer wavelengths of 12–40 km (corresponding to a depth of 12–48 km) [*Carbó et al.*, 2003; *Llanes*, 2006] (Figure 1c). A gravity minimum SW of El Hierro was also found and modeled by a negative density anomaly at a depth of 10 km by *Montesinos et al.* [2006].

In a field survey carried out prior to the 2011 unrest, *Gorbatikov et al.* [2013] studied the deep structure of El Hierro using microseismic sounding techniques. These authors found a central-eastern intrusive high-velocity body in the crust that they interpreted as being related to the early stage of the formation of the island, as well as a western intrusive body below the crust at a depth of >15 km that was interpreted as a recent magmatic reservoir (Figure 1d). This is consistent with the depth range of 19–26 km (in the upper-mantle) reported by *Stroncik et al.* [2009] for the magma plumbing and storage system in the upper-mantle below El Hierro.

After the 2011–2012 El Hierro eruption, *P* wave and *S* wave 3-D tomography was performed with the 13,000 local earthquakes registered from July 2011 to September 2012 [*García-Yeguas et al.*, 2014]. It revealed a high-velocity crust to a depth of 10–12 km and a low-velocity anomaly below the base of the crust, interpreted as a batch of magma rising as a small plume from the mantle located beneath El Hierro. Furthermore, recent *P* wave 3-D tomography [*Martí et al.*, 2017] performed with 20,000 local earthquakes registered in September 2011 to March 2014, revealed additional and valuable features. *Martí et al.* [2017] could model the structural complexity of the interior of El Hierro, including the identification of a number of stress barriers that authors interpreted as corresponding to regional tectonic structures and blocked pathways from previous eruptions, which reduces the options for fresh magma for finding a suitable pathway to the surface and for erupting (Figure 1e). These authors also confirmed the existence of a magma reservoir in the upper-mantle, situated in the central area of the island.
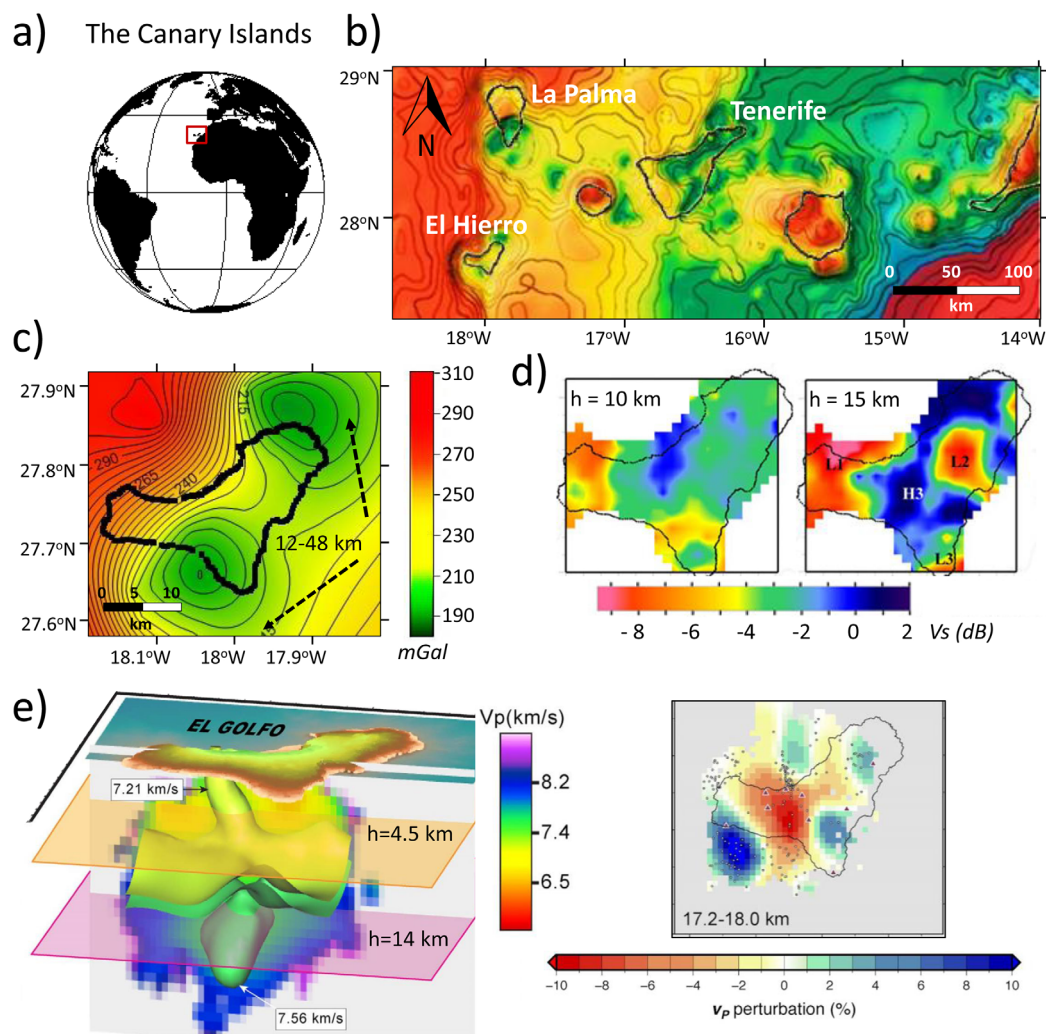
Figure 1. El Hierro location and its internal structure. (a) Geographical location of the Canary Archipelago. (b) Distribution of the islands over the Bouguer anomaly map (modified from *Carbó et al.* [2003] and *Llanes* [2006]), and (c) zoom of the local structures around El Hierro (color scale, in mGal, is the same in Figure 1b). (d) S wave velocity distribution at 10 and 15 km depth (modified from *Gorvatikov et al.* [2013]). (e) P wave 3-D tomography of the structure of El Hierro, and its horizontal projection at 17.2–18 km depth (modified from *Martí et al.* [2017]).

1.2. El Hierro Unrest

The unrest on El Hierro began on 19 July 2011 with the observation of low-magnitude seismicity located first in the central part of the island and subsequently migrating to the south at a depth of ∼9–16 km [*López et al.*, 2012; *Domínguez Cerdeña et al.*, 2014]. A simultaneous surface deformation confirmed the southward migration of the source of pressure [*Meletlidis et al.*, 2015]. Two weeks before the eruption (from 27 September onward), a clear acceleration in this process was registered with an increase in the rate of deformations and in the scale of the seismicity. Previous geophysical interpretations [e.g., *González et al.*, 2013; *Lopez et al.*, 2014; *Sainz-Maza et al.*, 2014; *Meletlidis et al.*, 2015] suggested that the final magma migration from depth to the surface could have started some days before the beginning of the eruption; however, the mechanism involved is unknown. On 8 October 2011, a *Mw* 4.0 earthquake, occurred 1.5 km off the southwest coast of the island. From this event to the beginning of a volcanic tremor signal on 10 October 2011 (04:10 UTC), the only recorded activity consisted of a few shallow (1–3 km depth) and low magnitude (<2 *Mw*) earthquakes occurring 5 km south of the island [*López et al.*, 2014].

Figure 2 shows the seismicity located by the IGN monitoring network (Figure 2a), the evolution of the located hypocenters (Figure 2b) and the double-couple focal mechanism solutions of the $M_W \geq 3.5$ events located during the unrest, all registered during 27 September to 9 October [*del Fresno*, 2016] (Figure 2c).
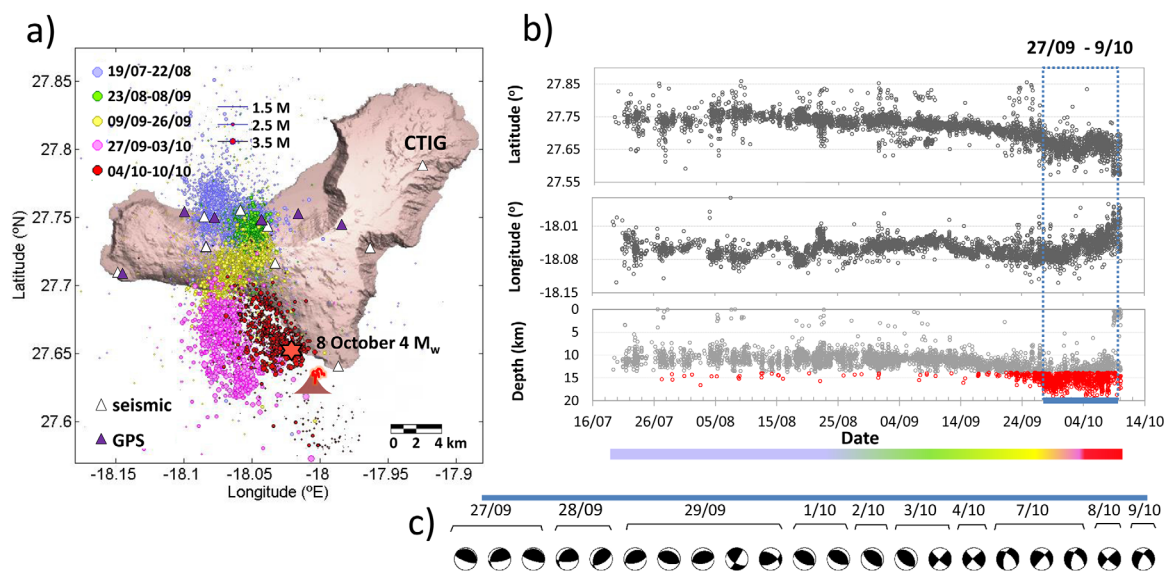
Figure 2. Seismicity located on El Hierro during the unrest. a) Distribution for different time periods; (b) evolution of hypocenter coordinates. Scale bar (purple: 19 July–22 August, green: 23 August to 8 September, yellow: 9–26 September, pink: 27 September to 3 October, red: 4–10 October). (c) Double-couple focal mechanism solutions of the $M_W \geq 3.5$ events in the period 27 September to 9 October. Seismic stations are represented by white triangles and GPS stations by black ones.

From 19 July to 8 September 2011, activity consisted of low-magnitude earthquakes located in clusters, as highlighted by a precise double-difference relocation study that used data from 3500 (out of a total of 10,000 events) local earthquakes registered during the unrest [*Domínguez Cerdeña et al.*, 2014]. We distinguish two periods (9–26 September and 27 September to 3 October) during which the seismicity of increasing magnitude was located to the south of the previous activity. Finally, high-magnitude sparse seismicity occurred on 3–10 October (including the 8 October 4.0 *Mw* earthquake).

2. Methodology and Analyses

We performed seismic and deformation characterization based on (1) temporal variations in the *b* value of the Gutenberg-Richter distribution and the *Vp/Vs* ratio; (2) the evolution of the accumulated seismic strain and seismic volume; (3) the characterization of the different seismovolcanic signals and the tensile-shear type of the fracturing; and (4) the modeling of the geodetic pressure sources for different time periods.

The seismic data were provided by the IGN catalog (www.ign.es) and includes the activity registered by the permanent seismic stations installed on El Hierro: one three-component (3CC) broadband station and eight short-period and medium-period 3CC stations (Figure 2a). Despite its low density, this network was well distributed and had a mean error of 3 km for epicenter location and 5 km for depth estimation [*López et al.*, 2012]. The local GPS network during the unrest episode had up to six stations, which allow daily coordinate solutions to be calculated. Although they registered data for almost the whole of the unrest episode, the distribution of these stations was uneven and only covered properly the north and central parts of the island (Figure 2a).

2.1. Seismic *b* Value and *Vp/Vs* Ratio Temporal Evolution

We calculated the variations in the *b* value of the Gutenberg-Richter law (see Appendix A1) to identify different time periods in which tectonic (driven mainly by tectonic plate activity) or volcano-tectonic (driven by the volcanic activity) seismicity predominated. We adjusted the unknowns, *a* and *b*, using the maximum curvature method [*Aki*, 1965] in overlapping moving windows with 200 earthquakes. We then computed the completeness magnitude (above this magnitude the catalog should include all the events recorded by the seismic network), Mw_C, and the maxima magnitude reached, Mw_{max}, in each time period [ZMAP program; *Wiemer*, 2001].

In addition, we analyzed the temporal variations in the *P*-(compressional) and *S*-(shear) wave travel time velocities (*Vp/Vs*) of the local earthquakes on El Hierro. In volcanic areas, the *Vp/Vs* ratio aids the study of

the properties of the medium, the existence of fluids and/or increasing/changing crack distribution, thereby identifying the volcano state and its evolution [e.g., *Lin and Shearer*, 2009; *Hong et al.*, 2014]. We calculated the Vp/Vs ratio and Poisson's ratio, ν, using the phase information (P wave and S wave arrival times) of the located and a robust multilinear regression for those $Mw > 1.7$ events in nonoverlapping windows with 300 earthquakes (see Appendix A1). P wave and S wave arrival times were manually picked (with an error less than 0.5 for P wave and 1 s for S wave) and hypocentral solutions were computed using a three layer velocity model based on a previous study of the Canary Islands [*Domínguez Cerdeña et al.*, 2014].

2.2. Seismic Strain and Volume

By applying the formulations in *Kostrov* [1974], *Jackson and McKenzie* [1988], and *Stich et al.* [2006] (see Appendix A2), we calculated the permanent seismic strain (static seismic deformation in response to stress forces) from the seismic moment (which measures the size of the earthquake, and is proportional to the product of the rock strength, the fault area, and the amount of slip) for different ranges of time and magnitude. We summed the contributions to the strain of the located seismicity (included in the seismic catalog) with magnitudes above Mw_C to the contribution of the seismicity with magnitudes below Mw_C (most of them not included in the seismic catalog) inferred from the b value regression of the Gutenberg-Richter distribution. This noncataloged seismicity is relevant when large earthquakes do not dominate the deformation ($b > 1.5$). We used the relationship established by *Hanks and Kanamori* [1979] between the scalar seismic moment, Mo, and Mw, $M_o = 10^{1.5Mw+9.05}$, and the a, b, Mw_{max}, and Mw_C values obtained in 2.1, with $Mw_{min} = 1.0$, the seismic consistency $Cs = 1$ and the shear modulus $\mu = 4 \times 10^{10}$ Pa [*Watts*, 1994; *Watts et al.*, 1997].

We estimated the contribution of the permanent seismic deformation (static deformation) to the variations in the volume from Mo using the approximation $\Delta V = \dfrac{\sum Mo}{\mu}$ [*Aki and Richards*, 1980; *Hill et al.*, 2003]. With this equation, $\sum Mo$ becomes proportional to the volume of the active fractures associated with the magmatic activity. In fact, for hydraulic fracturing or geothermal exploration projects this parameter allows operators to assess the extent of the stimulated rock volume and the efficiency of the injection activities [*Maxwell et al.*, 2006; *Shapiro et al.*, 2011].

2.3. Type of Seismic Signals and Tensile-Shear Fracturing

The continuous raw waveform includes a wide variety of seismic signals: transient signals such as volcano-tectonic events and low-frequency events and continuous signals such as microseismicity, volcanic tremors and swarms of volcano-tectonic events. To study the different contribution of these seismic sources to the seismic data acquired, and to discriminate weak seismic signals from noise, we performed a Real-time Seismic Amplitude Measurement (RSAM) analysis. The RSAM analysis is a robust tool for monitoring volcanic activity because it provides a simple indicator of the level of seismic energy released [*Endo and Murray*, 1991].

We calculated the RSAM (see Appendix A3) on the broadband CTIG seismic station (the CTIG was the only station with a flat instrumental response in the whole frequency spectra that recorded the seismic activity from the beginning to the end of the unrest). We separated the different seismic sources by applying bands filters to the continuous data: 1–3 Hz for tremors, low-frequency events (LF), hybrids and medium magnitude volcano-tectonic events (VT); 3–15 Hz small VT; and 15–30 and 30–50 Hz for very small and microseismic events, as per the classification in *Wassermann* [2012]. We corrected for instrument response and for attenuation, Q, (which is frequency-dependent). We adopted for the local S wave attenuation ($Qs = 90 * f^{0.5}$) the average of the values calculated by *Núñez* [2017] for El Hierro crust. The P wave attenuation, Q_P, was calculated using the *Knopoff* [1971] approximation, $Q_P \approx 2.25 * Q_S$. We also corrected data for geometrical spreading using a $(1/r)$ dependence of amplitude with the source-receiver distance, r. The P wave RSAM was computed using the vertical component and the S wave RSAM using the average sum of the NS and EW components.

After performing the RSAM on the S waves and P waves, the computation of the ratio between the energy in the S-radiated and P-radiated fields, E_S/E_P, was straightforward, and provided valuable information about the dominant fracturing type associated with the emplacement and migration of the magma.

2.4. Modeling of the Geodetic Pressure Sources and the Strain and Stress Fields

The GPS data were processed using Bernese software [*Dach et al.*, 2015] in the ITRF2008 reference frame and a network of more than 30 GPS stations located in the Canary Islands, Azores, North Africa, and southern Spain. Precise satellite orbits and absolute antenna-phase center models from the IGS, along with ocean-loading model FES2004, were applied [*Benito-Saz et al.*, 2017].

Three-dimensional displacements and their associated errors were calculated for each selected time period and inverted using the dMODELS software package [*Battaglia et al.*, 2013], which uses a nonlinear inversion algorithm to determine the best fit parameters (i.e. location, depth, and volume change) for the deformation source. We used the spherical source model within an elastic, isotropic, and homogeneous half-space [*McTigue*, 1987] with $v = 0.25$ and $\mu = 40$ GPa [*Watts*, 1994; *Watts et al.*, 1997]. To assess the uncertainty of the source model parameters, an empirical bootstrap method was applied 1000 times to estimate the 95% confidence intervals [*Efron and Tibshirani*, 1986]. Despite the simplicity these models provide a first-order analysis of the deformation sources and their evolution over time. As well, we calculated the static stress changes caused by the static displacement associated with the point pressure sources, following *Okada*'s [1992] formulation [Coulomb 3.3 software, by *Lin and Stein*, 2004; *Toda et al.*, 2005]. We modeled the static stress changes (see Appendix A4) using Young modulus $E = 100$ GPa and $v = 0.25$.

3. Results

The characterization analysis of the located seismicity showed significant variations of the Catalog performance. Figure 3 shows the time evolution of the *b value*, Mw_{max}, and Mw_C parameters (Figure 3a), the time evolution of the earthquake location on a N-S projection (Figure 3b), the time fluctuations of the Vp/Vs ratio (Figure 3c), and the Poisson's ratio curve (Figure 3d). Variation in Mw_C with time is immediately obvious (Figure 3a), especially during the intense seismic swarm episodes registered during the 2 weeks before the onset of the eruption. During seismic swarms most of the seismic waveforms were partially overlapping, thereby making the phase detection and separation of the earthquakes difficult or impossible. The incompleteness of the IGN catalog motivated us to use an approximate method for quantifying the contribution of the nonlocated seismicity that was not included in the seismic catalog (section 2.2).

Figure 4a shows the seismic strain time evolution corresponding to the located (above Mw_C) and nonlocated seismic events, the accumulated seismic volume (Figure 4b), and the daily $Mw \geq 2.5$ seismic events located by the IGN (Figure 4c).

In addition, given that the seismic catalog only includes volcano-tectonic seismicity above the Mw_C, we studied the continuous seismic waveform to try to extract additional information regarding the fracturing mechanism. Figure 5a shows the time evolution of E_S/E_P. P wave RSAM curves for different frequency bands are shown in Figures 5b and 5c.

We also analyzed and modeled the ground surface deformation recorded by the GPS network. Figure 6 shows the spherical source solutions corresponding to the following time periods: 31 July to 8 September (Figure 6a), 9–21 September (Figure 6b), and 22 September to 9 October (Figure 6c), within this final period an additional inversion for 3–9 October (Figure 6d). We selected these time periods to ensure that the resolution on the displacement measurements was sufficient, to minimize inversion errors, and to replicate as closely as possible the periods used in the seismic analyses. As only four-to-six GPS stations were operating during these time periods, and given that most were in the northern part of El Hierro, we employed a spherical source model. Therefore, we should consider the results simply as a first approximation of the deformation source, useful only for tracking and evaluating the evolution of the magma (volume change and position) during the unrest. However, other source geometries, heterogeneities of the crust or topography of the island should also be considered if more accurate results are required [e.g., *Masterlark*, 2007]. The results are summarized in Table 1, and include the location, depth, volume change, and chi-square per degrees of freedom (χ^2_v) for each of the spherical sources, together with the lower and upper limits of the 95% confidence intervals obtained by bootstrapping techniques.

Figure 6e shows the Coulomb static stress changes (modeled with the 3–10 October Mogi's source) (Table 1) on the specific faults corresponding to the 4.0 *Mw*, 8 October plane solution (295° strike; 40° dip; 164° rake) [*del Fresno et al.*, 2015].
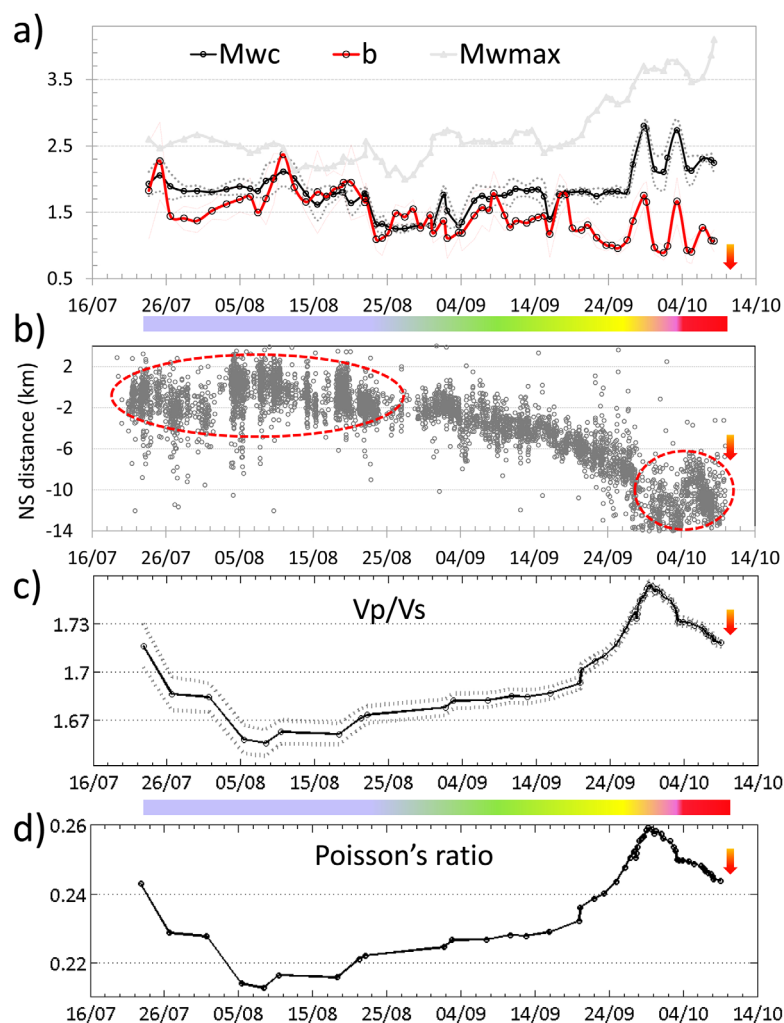
Figure 3. Main features of the located seismicity on El Hierro Island during the 2011 unrest. (a) Time evolution of the Mw_{max}, Mw_C, and b value parameters. (b) N-S growth distance from 19 August to 10 October (82 days), (c) Vp/Vs ratio evolution and error bounds, (d) Poisson's ratio evolution. Scale bar intervals as in previous figure. Vertical arrows indicate the onset of the eruption.

We noticed that the modeled spherical sources were always shallower than the seismicity and lay slightly further to the south in the direction of the seismic migration. This bias could be partially caused by intrinsic errors due to model simplification and the sparse GPS data used for the inversion. Another possible reason for these differences is that the seismicity accompanying dyke propagation in basaltic volcanoes represents events located backward with respect to the dyke tip position [*Traversa et al.*, 2010]. Moreover, the seismicity is not only related to the magma propagation but also to the response of the edifice itself to the volumetric deformation [*Traversa et al.*, 2010].

4. Discussion

Based on the results obtained here we discuss the emplacement and migration mechanism used by the magma on El Hierro to fracture and travel through the crust from its base to the Earth's surface.

4.1. Magma Emplacement

To discuss this issue, we applied hydraulic fracture theory—which offers a valuable tool for the interpretation of what occurs when a fluid (including magma) opens and fractures rock—to our results. When an over-pressurized fluid is injected into a volume of rock, the pressure migrates through the pores (pore pressure pulses) and stress variations in the rock occur (due to the opening and fracturing of fluid-filled cracks)
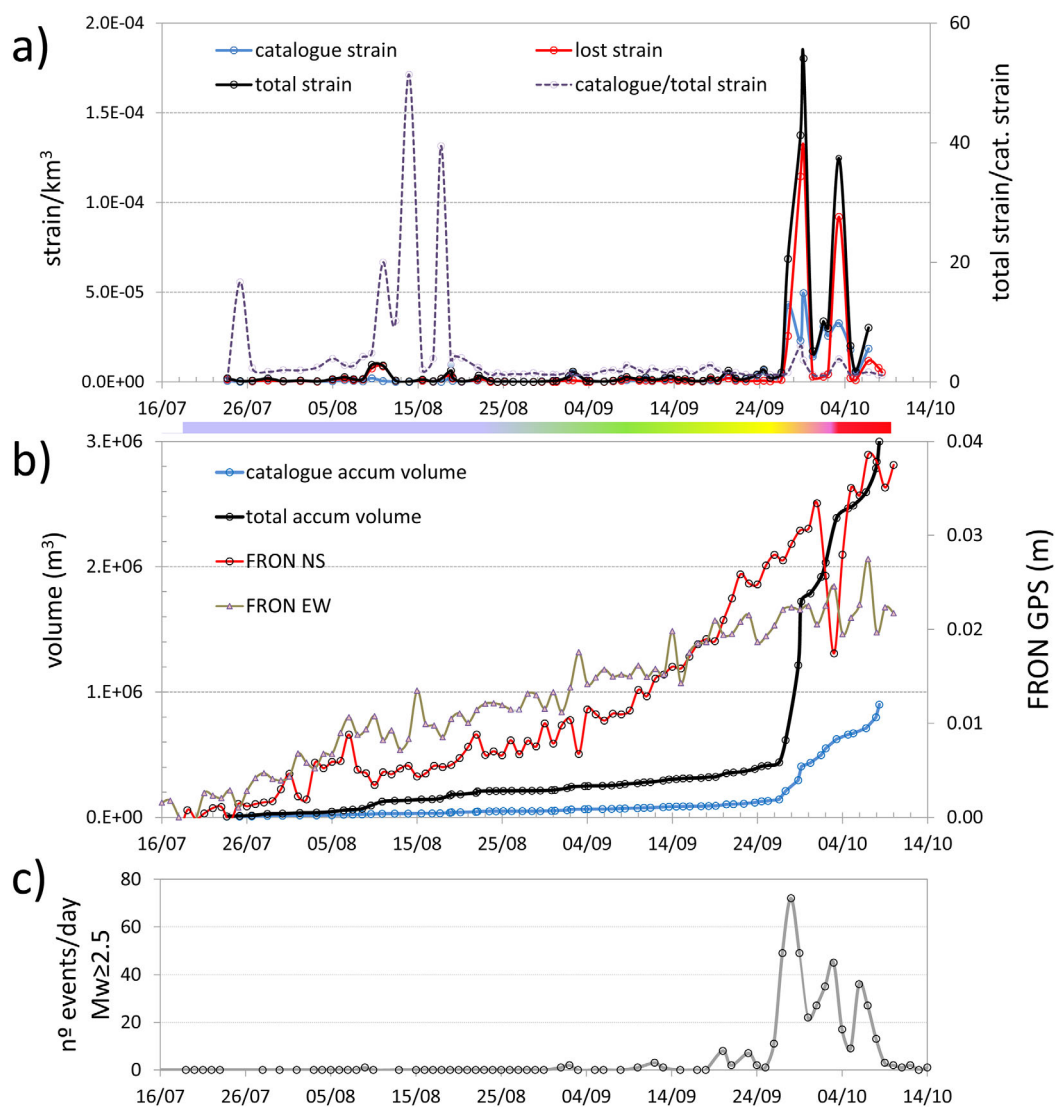
Figure 4. Strain analysis on El Hierro Island during the 2011 unrest. (a) Seismic strain of the located earthquakes above Mw_C (blue curve), below Mw_C (in red), the sum of both (in black) and rate of located strain to total strain (in purple). (b) Contribution to the volume of the earthquakes above Mw_C (in blue), total contribution from located and not located (in black) and horizontal (NS and EW) daily series from the FRON GPS station. (c) Number of $Mw \geq 2.5$ events per day. Scale bar intervals are as in previous figure.

[e.g., *Shapiro et al.*, 1997; *Miller et al.*, 2004; *Toda et al.*, 2002; *Dahm et al.*, 2010]. In the fluid-filled crack opening and fracturing model [e.g., *Dahm et al.*, 2010] cracks grow bidirectionally during the fluid injection process. This bidirectional growth continues for some time (postinjection) due to decompression by the remaining driving pressures, and then subsequently initiates unidirectional growth that is maintained depending on the stress gradients and the injection fluid pressure.

High *b* values (in some cases up to 2 or even 3) in volcanoes have been interpreted as being caused by the fracturing produced by fluid/magma intrusion in the mapping areas surrounding magma bodies [e.g., *Wiemer and Wyss*, 2002; *McNutt*, 2005; *Bridges and Gao*, 2006, *Murru et al.*, 2007; *Díaz-Moreno et al.*, 2015]. Additionally, several studies have highlighted how fluids, crack density and pore pressure influence the Vp/Vs ratio. Laboratory measurements [*Dvorkin et al.*, 1999] have shown that crack opening in rock samples induced by increasing pressure in gas-enriched pores leads to decreasing Vp/Vs ratios. Anomalous Vp/Vs ratios have also been registered in many volcanoes and low ratios are interpreted as an increase in the presence of gas in fractures [e.g., Kilauea, *Johnson and Poland*, 2013; Mount Etna, *Patanè et al.*, 2006; CampiFlegrei Caldera, *Chiarabba and Moretti*, 2006; Aso Caldera, *Unglert et al.*, 2011]. These authors suggest that
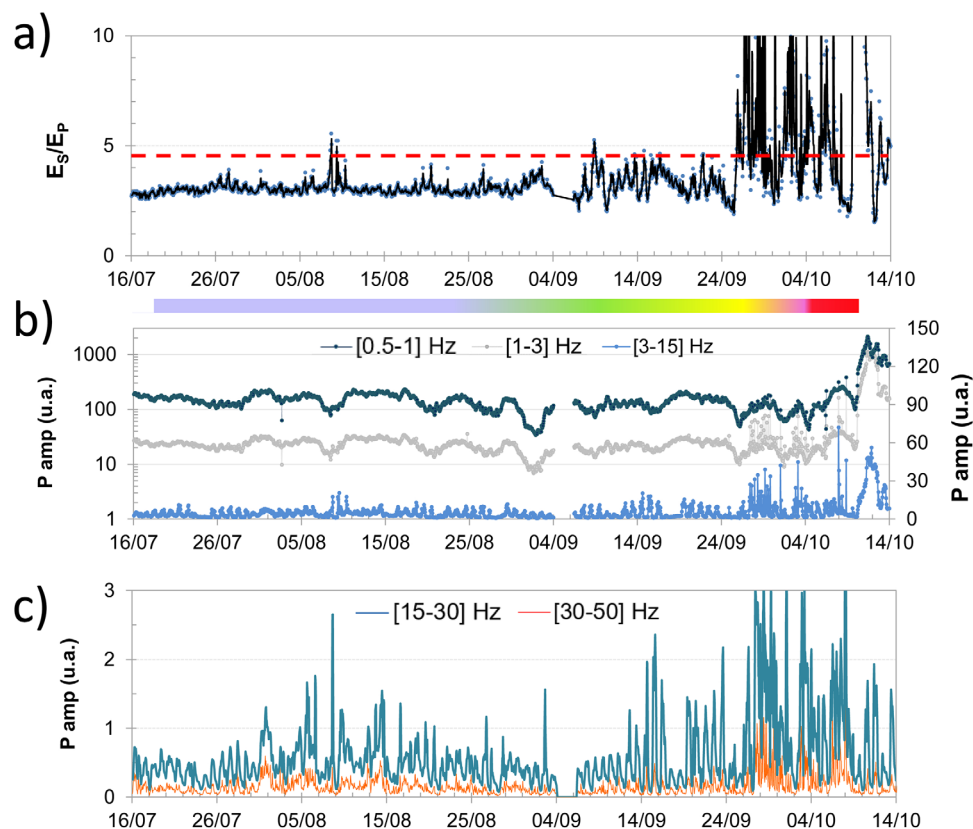
Figure 5. RSAM and tensile/shear type of fracturing analyses. (a) E_S/E_P time evolution. RSAM plots in P wave amplitude of the CTIG station for different frequency bands: (b) 0.5–1, 1–3, and 3–15 Hz and (c) 15–30, 30–50 Hz. Scale bar intervals as in previous figure.

increasing crack density should lead to higher S wave delay times and to lower Vp/Vs ratio values—if the cracks fill with gas.

The activity registered on El Hierro from the beginning of the unrest to when the seismic migration to the south at a constant depth started (19 July to ∼21 August) presented clustered swarm activity, low Mw_{max}, $b \geq 1.5$, tensile fracturing (low E_S/E_P ratio), low Vp/Vs ratio (low Poisson's ratio) and microseismicity. Based on hydrofracturing models, a fluid injection close to the crust-mantle discontinuity would explain the bidirectional seismicity growth, the b values, the clustered seismicity and the existence of seismic back-fronts and fore-fronts. The high $b > 1.5$ values and decreasing Vp/Vs ratio values would reflect the existence of crack opening and fluid-filled activity (gas-enriched). Nevertheless, variations in the Vp/Vs ratio cannot be attributed to any variation in depth in the fracturing since the seismicity depth range remained stable, thereby supporting the hydrofracturing (mainly tensile) origin of the seismicity registered from 19 July to ∼21 August. This fluid intrusion could not ascend through the crust due to the high-velocity crust in the area, as revealed by the two P wave and S wave tomography results [*Gorvatikov et al.*, 2013; *Martí et al.*, 2017] (Figure 1); instead, we infer that it over-pressurized the entire island and promoted extension and tensile fracturing of preexisting faults. The injection of magma into a preexisting mantle reservoir is supported by petrological data [*Longpré et al.*, 2014]. The observation of a spatial CO_2 positive flux anomaly in a faulted area in the north of El Hierro on 22 July–14 August [*López et al.*, 2012] could be congruent with this described state.

The seismic migration pattern observed from 21 August to ∼27 August suggests unidirectional growth in the fluid injection, with the growth being driven by structural or regional stress gradients. In this sense, the exact coincidence between the unidirectional growth path and the lateral heterogeneity at 10–15 km below the Moho discontinuity is notable [*Gorbatikov et al.*, 2013] on El Hierro (Figure 1). *Díaz et al.* [2015] also suggest the existence of stress diffusion and hydraulic fracturing in the seismic activity in their analysis of the temporal and spatial distribution of the seismic activity occurring on El Hierro in 2011–2013.
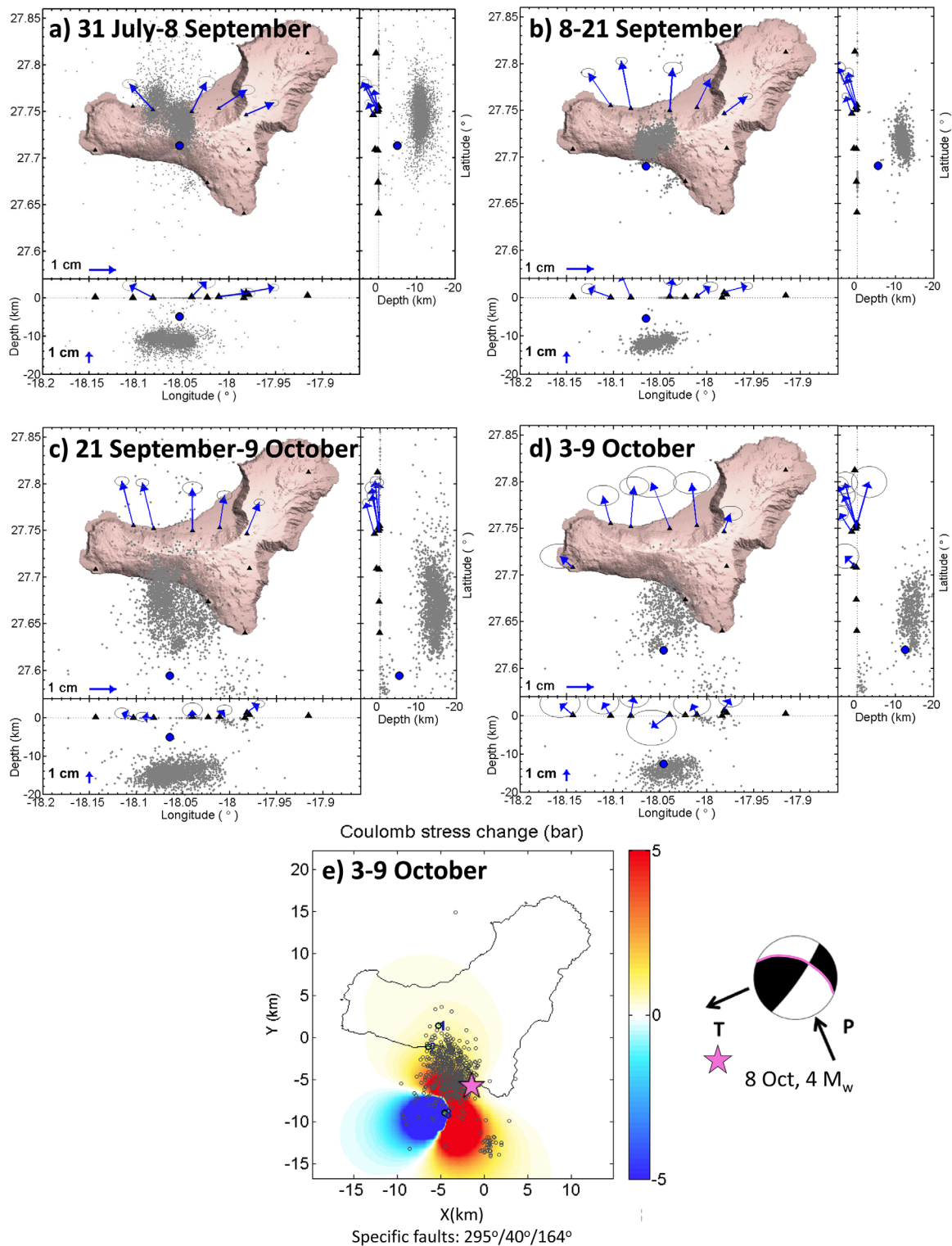
Figure 6. Location and depth of the spherical deformation sources for the selected time periods. GPS displacements are represented with blue arrows. (a) 31 July to 8 September. (b) 9–21 September. (c) 22 September to 9 October. (d) 3–9 October. (e) 3–9 October, Coulomb stress change (bar) distribution on (295° strike, 40° dip, 164° rake) faults at a depth of 12 km, and focal mechanism solution of the 4.0 Mw 8 October event (pink star).

4.2. Evidence of Increasing Magma Pressurization

On 21 and, more clearly, on 27 September, the activity changed drastically and from this date onward features appeared that had never been observed before at El Hierro: deeper earthquakes, very intense swarms

Table 1. Optimal Spherical Source Model Parameters (With 95% Confidence Intervals)

Time Periods	Longitude (°)	Latitude (°)	Depth (km)	ΔV (km³)	X^2_v
31 Jul 2011/8 Sep 2011	$-18.053^{-18.012}_{-18.140}$	$27.713^{27.730}_{27.629}$	$4.9^{14.0}_{2.3}$	$0.004^{0.030}_{0.001}$	4.7
8 Sep 2011/21 Sep 2011	$-18.065^{-17.990}_{-18.136}$	$27.690^{27.701}_{27.518}$	$5.4^{21.6}_{4.1}$	$0.008^{0.091}_{0.004}$	5.4
21 Sep 2011/9 Oct 2011	$-18.064^{-18.043}_{-18.092}$	$27.595^{27.599}_{27.504}$	$5.1^{11.6}_{4.2}$	$0.026^{0.060}_{0.023}$	6.0
3 Oct 2011/9 Oct 2011	$-18.047^{-17.971}_{-18.139}$	$27.620^{27.668}_{27.506}$	$12.6^{22.9}_{3.0}$	$0.027^{0.085}_{0.009}$	4.8

of VT events, alternation of b values minima close to 1 with maxima of $b \sim 1.5$, alternation of shear and tensile behavior, maximum Poisson's ratio values, maximum seismic strain release, and the greatest deformation, as reflected by the higher modeled Mogi's source volume. This activity occurred in two pulses (27–30 September and 2–5 October) and was registered by the seismic and the GPS network. Figure 7 shows the time series of the GPS, the seismic strain and the evolution of Poisson's ratio. Of note are the coincidence between the coherent oscillation in the NS component and the seismic strain pulse (2–5 October) with maximum on 3 October, and the change in the focal mechanism from thrust fracturing to strike-slip that occurred on that date (top plot in Figure 7).

The variations in the Vp/Vs ratio from 27 September onward cannot be attributed clearly to any variation in the depth of the fracturing since the seismicity depth range remained stable (at least the seismicity located and included in the seismic catalog). Furthermore, at the maxima of these two pulses, the E_S/E_P values show shear fracturing and b values over 1.5, while at the minima, the E_S/E_P values show tensile fracturing and $b \sim 1$ (Figure 3a). Rapid variations in the deformation (inflation/deflation cycles) have been related to dyke propagation that allows the movement of magma and temporal changes in the local stress and strain fields [e.g., *Heimisson et al.*, 2015].

We cannot rule out a bias in the GPS coordinates during (3–5 September) due to atmospheric instabilities recorded by the meteorological stations on the island. As described in *Larson et al.* [2010], path delays caused by the troposphere are one of the most important sources of error in GPS precision. In addition, based on *Tregoning and Herring* [2006], poor Zenith Hydrostatic Delay values can corrupt the station coordinates and the Zenith Total Delay estimates; nevertheless, this effect is more significant in the vertical component than in the horizontal ones. Thus, we believe that the deformation was real and not biasedgiven that it was greater in its horizontal components than in its vertical ones (Figure 7) and that there were changes in the volcanic system detected by other techniques. However, the magnitude of the deformations on those days could have been influence by tropospheric effects.

When discussing the relationship that exists between tectonic stress fields and the earthquakes triggered by magma overpressure, *Roman et al.* [2007] propose different faulting scenarios that vary in terms of the strength of the regional tectonic stress compared to the volcanic stress. Faults slip in the direction of the regional maximum compression if regional stresses dominate; there is no faulting and shadow zones are created around the inflating dyke if regional stresses balance volcanic stresses; and reverse faulting occurs if volcanic stresses dominate [*Roman et al.*, 2007].

Regarding the Coulomb static stress changes associated with the modeled sphere pressure sources, both triggered seismicity and stress shadow have been observed in association with evolving static stress changes during propagating dyke mechanisms in active volcanoes [e.g., *Green et al.*, 2015]. The Coulomb stress at the site of the 8 October event (Figure 6e) was $\sim$5 bar. The focal mechanism of this event was modeled by *del Fresno et al.* [2015], who obtained a pure double-couple mechanism with a null isotropic (dilatational) component, which rules out any volume changes in the source due to magma intrusion. By modeling a circular fault model [*Brune*, 1970], *del Fresno et al.* [2012] calculated a rupture area of 0.9 km² and 20–30 bar for the stress drop. This stress drop is higher than the 5 bar (0.5 MPa) of positive change in the Coulomb stress; in preexisting faults similar variations provoke faulting, thereby provoking an earthquake [*Walter and Amelung*, 2006, *Chouet and Matoza*, 2013]. Thus, a positive stress transfer by itself could have triggered the 8 October 4.0 *Mw* earthquake along a preexistent fault, as well as other lower magnitude seismicity, as suggested by the close coincidence between the 3 and 8 October spatial location distribution and the area with greatest stress (in red) (Figure 6e).

Based on these observations, we suggest that from 27 September onward, an increase in over-pressurized melt, reached the mantle-crust boundary, in accordance with the reverse type of the focal mechanism. This
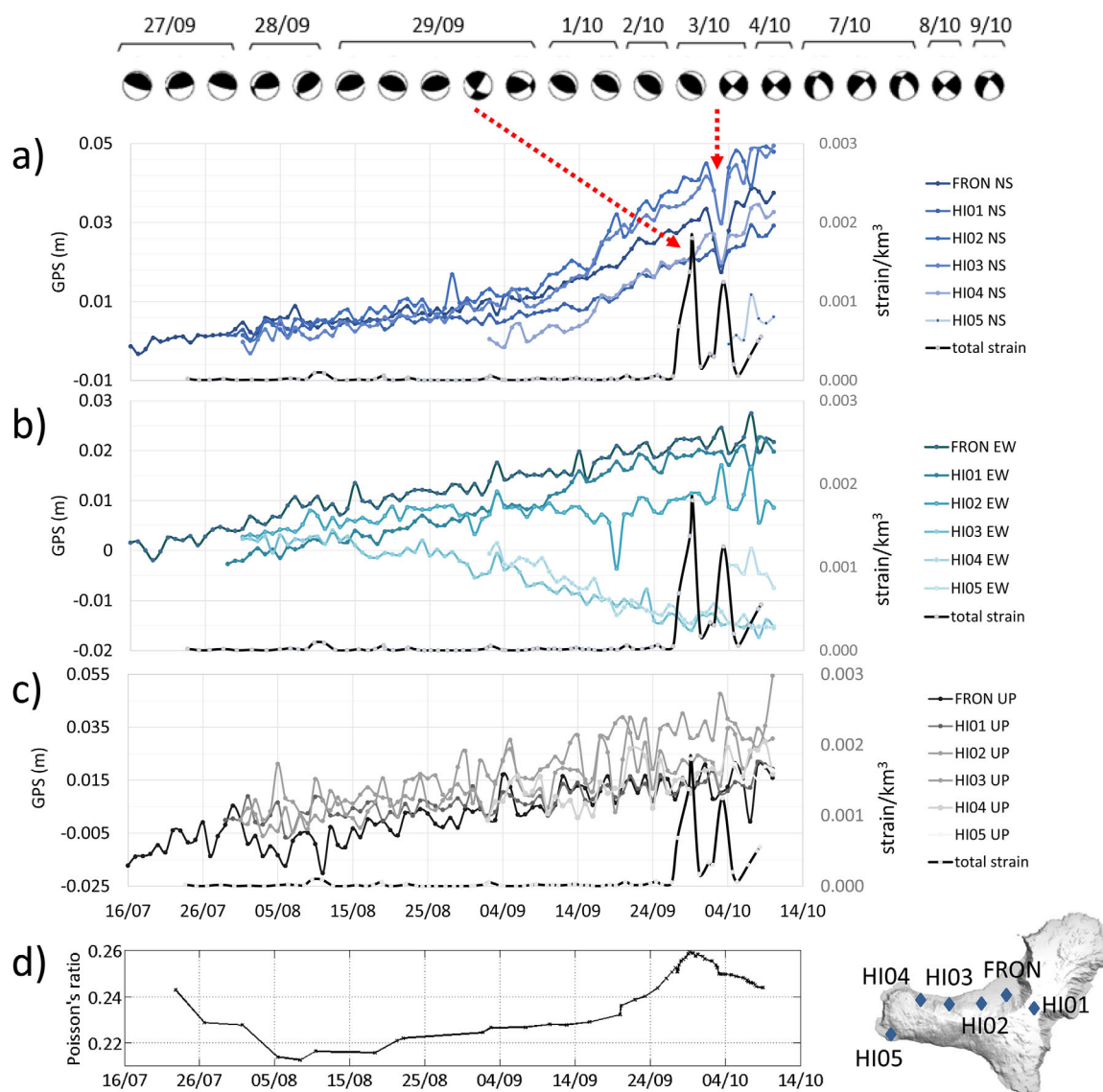
Figure 7. Comparison of the evolution of the seismic strain, the geodetic strain (time series of GPS deformation) and the Poisson's ratio during the 2011 El Hierro unrest. (a) GPS NS component and the seismic strain, (b) GPS EW components and seismic strain, (c) GPS vertical components, and seismic strain, (d) Poisson's ratio time evolution.

increased overpressure promoted tectonic seismicity while increasing in volume due to the tensile emplacement of additional melt material. During the reverse faulting period (27 September to 3 October), volcanic stresses probably dominated, the source of this fracturing being clearly located below the crust base (~12–5 km depth) [*Martí et al.*, 2017]. The change in focal mechanism and the GPS oscillation patterns registered around 3 October suggest that an important change occurred, probably due to the propagation of a dyke from the magma reservoir that caused a fall in the magma pressure below the crust. The strike-slip seismicity registered on 3–8 October could have been the consequence of increased Coulomb stress transfer on preexisting regional faults in the crust since strike-slip event planes coincided with the maximum regional NW-SE compression [*Geyer et al.*, 2016]. The rapid variations in the Vp/Vs recorded in this period probably reflect the abrupt changes in the stress and deformation states, which cause fracturing, and the active transport of fluids (melt) driving more fracturing in a positive feedback system that ultimately leads to the eruption [*Koulakov et al.*, 2012]. During the seismic quiescence registered after the occurrence of the 8 October 4 *Mw* event, an intermediate scenario could have occurred, whereby increasing volcanic stress balanced out the regional stress.

4.3. Geometry of the Upward Magma Migration

Martí et al. [2013] proposed a mechanistic model for the eruption on El Hierro by numerical modeling of the stress and the strain fields in an elastic lithosphere, including the effects of flexure, edifice load and the water layer. Their results explain some of the aspects and features observed during the unrest, including the lateral sill propagation of the magma below the crust and the lateral ascent toward the surface away from the edifice center. These authors suggest the presence of an intrusive complex characterized by different rheology that would explain the halt in the vertical progression of the magma when it reached the bottom of the crustal boundary [e.g., *Gudmundsson*, 2006].

Here we complement the mechanism by applying the conditions for tensile and shear fracturing in monogenetic volcanism [e.g., *Martí et al.*, 2016] (see Appendix A5). For the crust failure, the magma pressure needs to reach values over $10–200 + \sigma_n$ to create new fractures under the normal stress (σ_n) or greater than $1 + \sigma_n$ bar to open a preexisting fault. In the case of tensile faulting ($\sigma_n < 0$), the pressure required will be lower [e.g., *Gudmundsson*, 2012; *Martí et al.*, 2016]. Therefore, it is evident that, in the event of low-pressure conditions, the most probable scenario is the emplacement of magma into previously faulted areas of the crust because of tensile opening. As the stress drop after a tensile earthquake is smaller than in the case of shear failure volcanic earthquakes associated with tensile failure will have small magnitudes and the radiated seismic waves will have more energy at higher frequencies. This was probably the case of the high-frequency microseismicity registered during the El Hierro unrest in the periods in which tensile behavior was dominant (Figure 5c).

Figure 8 represents the results of the biaxial modeling [*Zang and Stephansson*, 2010] of the differential stress field and the magma pressure (ascending from a 3 MPa over-pressurized source located at a depth of
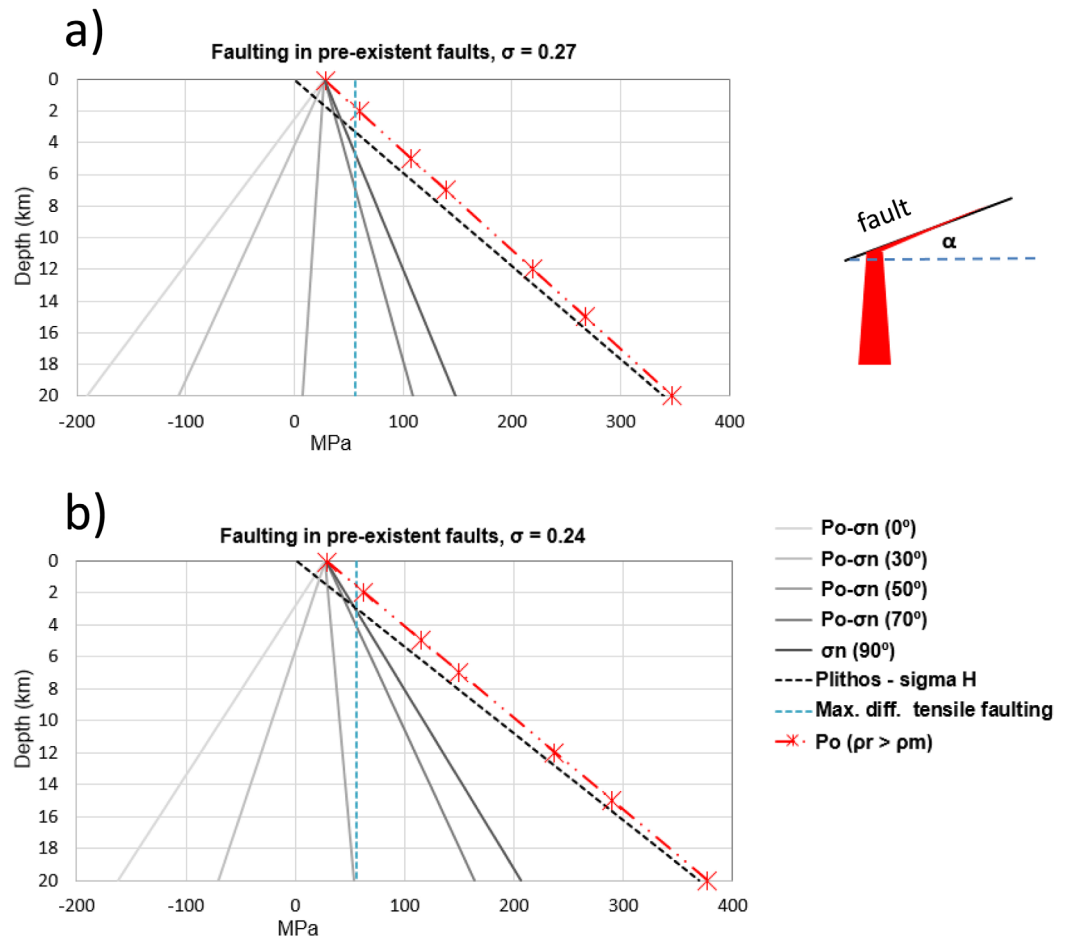

Figure 8. Magma overpressure in the fracture $P_{net} = (P − \sigma_n)$ for different dip angles, superimposing the maximum differential stress curve for the occurrence of tensile faulting (560 bar) for (a) $v = 0.27$ and (b) $v = 0.24$.
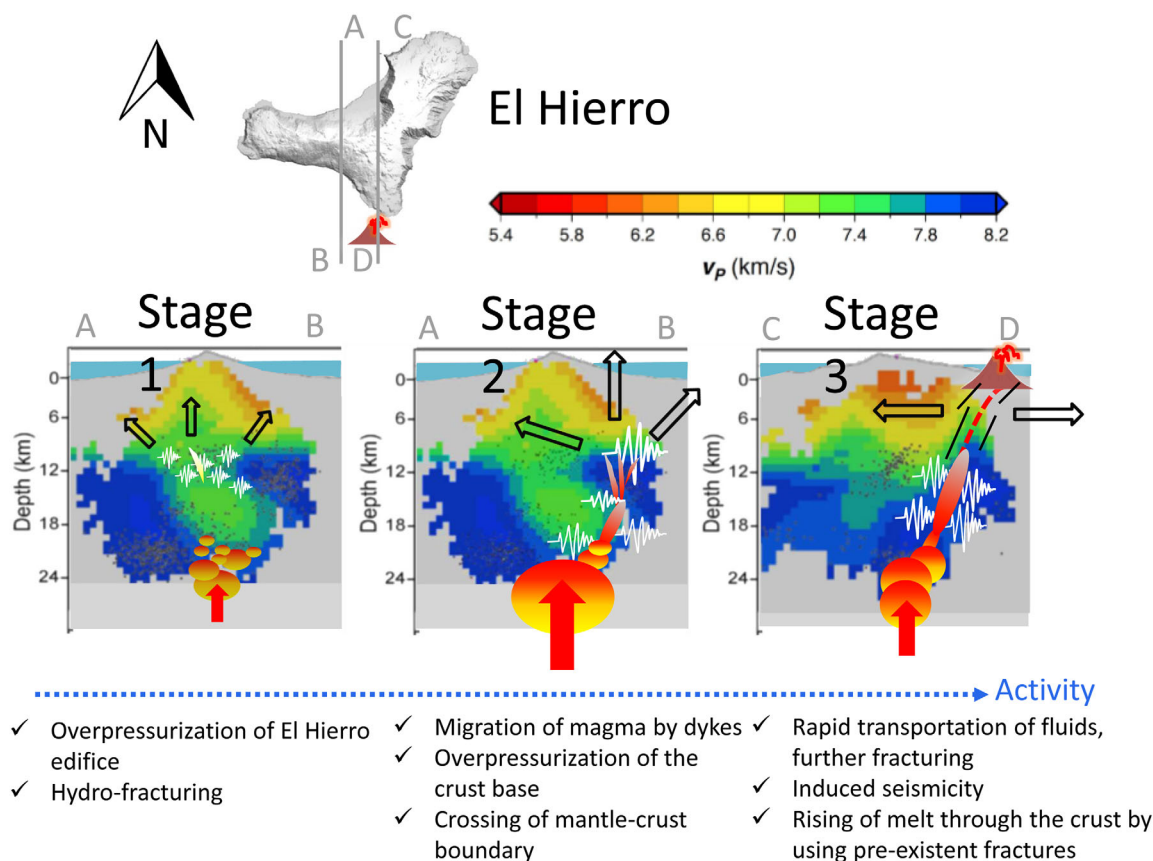
Figure 9. Conceptual model for the El Hierro volcanic unrest mechanism. Stage 1 (19 July to 27 September), Stage 2 (27 September to 3 October), Stage 3 (3–10 October). Vertical cross sections drawn over a modified version of the *P* wave tomography results [*Martí et al.*, 2017].

20 km). The overpressure in the fracture, $P_{net} = (P − \sigma_n)$, is calculated for different dip angles (see Appendix A5). We located the roof of the magma chamber at a depth of 20 km, in accordance with the modeled anomalous body found at that depth by *Marti et al.* [2017]. We used the same values for magma and crust densities as used by *Becerril et al.* [2013] in their numerical modeling of the feeder dykes on El Hierro: $\rho_m = 2.65 \times 10^3$ kg m^{-3} for the basaltic magma density and $\rho_r = 2.75 \times 10^3$ kg m^{-3} for the host crust. We used $v = 0.27$ (Figure 8a) and $v = 0.24$ (Figure 8b) that bound the Poisson's ratio values obtained from the seismic catalog analysis. Our modeling shows that the requirement for induced vertical-plane tensile faults, $(\sigma_V − \sigma_H) < 560$ bar, is fulfilled at shallow depths (less than 3 km), and tensile openings are possible on fractures oriented within 22.5° from σ_V (Figures 8a and 8b). At any other depths in the crust and at other orientations, new fractures will be shear or tensile in nature but will occur in preexisting fractures. As the differential stress increases with depth and pore pressure, leading to smaller real differential stresses and a greater probability of a crack opening in over-pressurized formations [*Fischer and Guest*, 2011], we cannot rule out the possibility that tensile opening could occur near the magma reservoir or the dyke. One noticeable result is the influence of Poisson's ratio on the available faults planes that the over-pressurized magma uses to travel from depth to the surface. Whatever the case, at depths of less than 6–7 km, positive buoyant magma will open all preexistent faults at any dip angle.

Stress modeling highlights the importance of the preexisting faults on El Hierro. The lithosphere in the south of El Hierro could be faulted and coincide with the known low-density and gravity anomaly [*Carbó et al.*, 2003; *Gorvatikov et al.*, 2013]. Once the magma crossed the Moho south El Hierro, dyke stress would unclamp the preexisting faults, thereby allowing the aperture of a magma path to the surface in a combined process of tensile and shear fracturing. During its migration, the geometry and orientation of the dyke changed to take advantage of new available fault planes (Figure 8), which gave rise to apparently aseismic migration close to the surface on 8–10 October, probably due to high-aperture tensile fracturing. This stagnation of the magma in the lower crust and the lateral propagation have been also described in previous petrological studies focusing on the olivine crystals [e.g., *Longpré et al.*, 2014].

4.4. Conceptual Model

Finally, we provide a conceptual model (Figure 9) for the unrest mechanism in which three main stages can be distinguished:

Stage 1: Magma injection overpressures the existing magma reservoir below the crust, promoting stress diffusion and hydraulic fracturing of preexisting and new cracks in the lower crust (∼9–15 km) [*Martí et al.*, 2017] with gas-enriched fluids. Regional fields control the migration of the stress perturbation involved in the fracturing to the south.

Stage 2: Over-pressurized magma pulses reach the crust base by migrating to below the Moho discontinuity. Increased overpressure promotes tectonic seismicity, while the reservoir increases in volume due to the tensile emplacement of additional melt material. During the reverse faulting period (27 September to 3 October) volcanic stresses were probably dominant, the source of this fracturing clearly being below the crust base. The high-velocity crust base blocked upward dyke propagation. This stage finished with the crossing of the mantle-crust boundary in a faulted crust region south El Hierro.

Stage 3. On 3–8 October, an increase in the transport of magmatic fluids in fractures led to greater fracturing of the lower crust in a positive feedback system. Dyke propagation caused a fall in the magma pressure below the crust and the increase in the stress in the crust. The positive stress transfer in the crust could have triggered seismicity along a preexistent fault on 3–8 October. An increasing volcanic stress balance with the regional stress field enabled the propagating dykes to use and maintain opening of the network of preexisting faults from the crust base to the surface. In the upward migration, the magma starts by using vertical preexisting faults and opens closer to the surface preexisting faults of any dip angle, thereby promoting during the final kilometers horizontal (lateral E-W oriented) migration that reached the surface far from the area in which the previous seismicity had been located.

5. Conclusions

Even though the data used were limited, the methods applied were an approximation of the physics involved in an eruptive event, and that the results include numerous uncertainties rather than simple solutions, the consistency provided by comparable results allows us to hypothesize how and why the eruption on El Hierro took place. Additionally, compared to previous studies that have employed some of the techniques used in this work (e.g., *b* value analyses, source modeling), we have been able to provide a complete calculation of the whole evolution of the seismic strain and the Coulomb modeling of the stress field changes. In a similar way, no *Vp/Vs* temporal evolution study or E_S/E_P characterization of the tensile/shear fracturing, or error analyses of the deformation sources, have ever been performed using the data set from El Hierro. Some of the evidence found is novel (e.g., occurrence of high-magnitude triggered seismicity, hydrofracturing by gas-enriched fluids, evidence of the crossing of the mantle/crust boundary), as is the interpretation of the overall evidence in light of the detailed knowledge of the structure of El Hierro.

It is also worth noting that when the seismic activity included in a seismic catalog does not include very low-magnitude seismicity (tensile fracturing), or when its performance is dependent on the seismic rate, only a very approximate (in the best of cases) path along which the magma is rising or accumulating can be drawn. High-magnitude activity can be partially related to the opening of the preexisting network of fractures of the volcano edifice and some of the high magnitude events are caused by stress triggering. Likewise, it is essential to have a dense GPS network for precise modeling of the magma intrusion and the changes in its geometry as it crosses the lithosphere. Otherwise, it is only possible to derive simple and probably biased models. Therefore, we stress the crucial importance of setting up a high-quality (i.e., dense, low-noise, well-distributed) network of instruments and developing new tools for comprehensive monitoring of volcanic activity and the correct interpretation of the observational data acquired.

APPENDIX A

A1. Seismic b Value and Vp/Vs Ratio Temporal Evolution

The Gutenberg-Richter (G-R) distribution power law states that,

$$log_{10}n(M)=a-bM, \tag{A1}$$

where $n(M)$ is the cumulative number of earthquakes of magnitude larger than M, a represents the earthquake productivity, and b describes their size distribution [*Gutenberg and Richter*, 1944].

The Vp/Vs ratio can be estimated by using a modified Wadati analysis [*Wadati*, 1933; *Jo and Hong*, 2013]:

$$\frac{Vp}{Vs} - 1 = \frac{(Ts - Tp)}{Tp},$$ (A2)

where T_P and T_S are the observer P wave and S waves phase readings.

From Vp/Vs, the Poisson's ratio v (the ratio of transverse contraction strain to longitudinal extension strain in the direction of stretching force) can be calculated using:

$$v = \frac{1}{2}\left[1 - \frac{1}{(Vp/Vs)^2 - 1}\right].$$ (A3)

A2. Seismic Strain

Kostrov's [1974] theorem states that the average seismic strain tensor can be defined by

$$\varepsilon_{ij} = \frac{1}{2\mu V}\sum_{n=1}^{N} M_{ij}^{n},$$ (A4)

where M_{ij}^{n} is the component ij of the seismic moment tensor M_n of the earthquake nth that occurred in the crustal volume V, (that contains the active faults), whose average elastic shear modulus is μ.

If the moment tensor solution is not available, the approximation of *Frohlich and Apperson* [1992] can be applied, which calculates the contribution of the scalar seismic moment of each individual earthquake, Mo, by

$$|\varepsilon| = \frac{1}{2\mu V} C_S \sum_{n=1}^{N} M_o^{n},$$ (A5)

where C_S is the seismic consistency and has a value $C_S \leq 1$. ε represents the amount of final permanent deformation accommodated within the considered crustal volume. If we compute ε for the seismicity occurred over a period of time, Δt, we can refer to the result as $\dot{\varepsilon} = \varepsilon/\Delta t$, the average seismic strain rate. We can compute the average strain between a range of magnitudes Mw_1 and Mw_2 by

$$\int_{Mw_1}^{Mw_2} \frac{d|\varepsilon|}{dM_W} = \int_{Mw_1}^{Mw_2} \frac{C_S}{2V\mu} n(M_W) M_0 dM_W.$$ (A6)

This equation allows us to compute the contribution of the located seismic events from the completeness moment magnitude $Mw_1 = Mw_C$ to the maximum moment magnitude of the catalog $Mw_2 = Mw_{max}$. The ratio of the integration of (6) for adjacent magnitude intervals is

$$\frac{|\varepsilon|_{Mw0 - Mw1}}{|\varepsilon|_{Mw1 - Mw2}} = \frac{10^{(1.5 - b)Mw_1} - 10^{(1.5 - b)Mw0}}{10^{(1.5 - b)Mw_2} - 10^{(1.5 - b)Mw_1}}$$ (A7)

This equation allows us to compute the contribution of the nonlocated earthquakes, from an a priori minimum moment magnitude $Mw_0 = Mw_{min}$ to $Mw_1 = Mw_C$.

A3. RSAM Analysis

The RSAM analysis [*Endo and Murray*, 1991] is defined by

$$RSAM = \frac{\sum_{i=1}^{n} |A_i - \bar{A}|}{n},$$ (A8)

where A_i, is the signal amplitude corrected by the instrument response and the geometric and anaelastic attenuation occurred from the hypocenter to the station; $\bar{A}$ is the mean amplitude in the calculation window and n is the number of samples in the window.

The RSAM analysis is an approximated method for computing the continuous scalar seismic moment, Mo, and allows us to study the fracturing mechanism associated with the magmatic activity in the case of

continuous or overlapping seismic signals. This approximation is more rewarding when the magnitude of the earthquakes decreases—thereby hindering their detection and location—during dense earthquake swarms, or when the magnitude of completeness is high. Following the description of the source radiation function of *Aki and Richards* [2002], *Mo* can be estimated from the far-field seismic *P* waves and *S* waves displacement recording, *u* (*x,t*). In a homogeneous whole space

$$u(x,t) = \frac{R^{P,S}}{4\pi\rho V^3 r} \dot{Mo}\left(t - \frac{r}{V}\right), \tag{A9}$$

$$Mo = \frac{4\pi\rho V^3 r \int_{t_1}^{t_2} u(t)}{R^{P,S}}, \tag{A10}$$

where ρ is the rock density, *V* is the *P* wave or *S* wave velocity, *r* is the source-receiver distance, $\dot{Mo}$ the seismic moment rate, and $R^{P,S}$ is the *P* wave and *S* wave radiation patterns. If no focal mechanism solution is available, the average radiation pattern correction, 0.44 for *P* waves and 0.60 for *S* waves, can be used [*Boore and Boatwright*, 1984]. The approximated mean scalar seismic moment, *Mo*, can then be estimated from (9) and (10) in the (*n* samples) t_1–t_2 window using the equation

$$nRSAM = \int_{t_1}^{t_2} u(t). \tag{A11}$$

A4. Coulomb Stress Calculations

The Coulomb failure criterion hypothesizes that failure is promoted when the Coulomb stress change is positive

$$\Delta\sigma_f = \Delta\tau_s + \mu' * \Delta\sigma_n, \tag{A12}$$

where $\Delta\sigma_f$ is the change in failure stress on the receiver fault, $\Delta\tau_s$ is the change in shear stress (positive when sheared in the direction of fault slip), $\Delta\sigma_n$ is the change in normal stress (positive if the fault is unclamped), and μ is the effective coefficient of friction on the fault. The strain and the shear and normal components of the Coulomb stress change can be calculated in an elastic half-space in specific faults (receiver fault planes) or on a 3-D grid [*Okada*, 1992; *Lin and Stein*, 2004; *Toda et al.*, 2005].

A5. Failure Criteria and Magma Pressure on a Propagating Dyke

The 2-D Mohr-Coulomb failure criteria states that new tensile opening will occur along fractures oriented within 22.5° from σ_1 (greater stress component) if the differential stress $(\sigma_1 - \sigma_3) < 2\sqrt{2}S_0$, where σ_3 is the smallest stress component and S_0 the rock cohesion. If both conditions are fulfilled the rock will fail in tensile mode or if not, in a shear or hybrid mode. For a typical rock cohesion of $S_0 = 200$ bar, the maximum differential stress for the occurrence of tensile faulting is $\sim$560 bar, although this value can be much smaller if there are preexisting fractures with significantly smaller cohesion [*Fischer and Guest*, 2011].

In a biaxial modeling [*Zang and Stephansson*, 2010] σ_1 is vertical and equals σ_V (lithostatic load) and σ_3 is horizontal. In a first approximation $\sigma_V = 250$ bars/km, while the horizontal or lateral stress is proportional to the vertical load depending on the material properties of the lithosphere [e.g., *Zang and Stephansson*, 2010; *Cañón Tapia*, 2013]

$$\sigma_H = k * \sigma_v = (\nu/(1-\nu)) * \sigma_v, \tag{A13}$$

with ν, the Poisson's ratio. This increasing stress is appropriate for describing the brittle oceanic lithosphere in general form, characterized by a single strength maximum. The normal stress along a fault, σ_n, for different fault dip angles, α, is defined by the equation $\sigma_n = \sigma_V cos^2\alpha + \sigma_H sin^2\alpha$. When a dyke approximates to a preexisting fault, the magma will open a preexisting fault that was closed by a normal stress, if the magma pressure $P_o \geq \sigma_n$. The overpressure in the new fracture $P_{net} = (P_o - \sigma_n)$ will be equal to the tensile rock strength, which in the laboratory assumes values from 10 to 200 bar for intact rock and $\ll$10 bar if there are preexisting fractures [*Fischer and Guest*, 2011]. The magma overpressure in a dyke, P_0, can be calculated using the equation [e.g., *Gudmundsson*, 2012; *Martí et al.*, 2016]

$$P_0 = p_e + (\rho_r - \rho_m)gh + \sigma_d, \tag{A14}$$

where p_e is the excess pressure in the magma reservoir, σ_d the differential stress at the level of the dyke $(\sigma_d = \sigma_V - \sigma_H)$, *h* the height of dyke above chamber, ρ_r and ρ_m the rock and magma densities and *g* the gravity acceleration.

References

Aki, K. (1965), Maximum likelihood estimate of b in the formula logN=a−bM and its confidence level, *Bull. Earthq. Res. Inst. Univ. Tokyo*, *43*, 237–239.

Aki, K., and P. G. Richards (1980), *Quantitative Seismology: Theory and Methods*, vol. 1, 557 pp., Freeman, San Francisco, Calif.

Albert, H., F. Costa, and J. Martí (2016), Years to weeks of seismic unrest and magmatic intrusions precede monogenetic eruptions, *Geology*, *44*(3), 211–214.

Battaglia, J., V. Ferrazzini, T. Staudacher, K. Aki, and J. L. Cheminée (2005), Pre-eruptive migration of earthquakes at the Piton de la Fournaise volcano (Réunion Island), *Geophys. J.*, *161*(2), 549–558.

Battaglia, M., P. F. Cervelli, and J. R. Murray (2013), dMODELS: A MATLAB software package for modeling crustal deformation near active faults and volcanic centers, *J. Volcanol. Geotherm. Res.*, *254*, 1–4.

Becerril, L., I. Galindo, A. Gudmundsson, and J. M. Morales (2013), Depth of origin of magma in eruptions, *Sci. Rep.*, *3*, 2762, doi:10.1038/srep02762.

Bell, A. F., and C. R. J. Kilburn (2011), Precursors to dyke-fed eruptions at basaltic volcanoes: Insights from patterns of volcano-tectonic seismicity at Kilauea volcano, Hawaii, *Bull. Volcanol.*, *74*, 325–339, doi:10.1007/s00445-011-0519-3.

Benito-Saz, M. A., M. M. Parks, F. Sigmundsson, A. Hooper, and L. García-Cañada (2017), Repeated magmatic intrusions at El Hierro Island following the 2011–2012 submarine eruption, *J. Volcanol. Geotherm. Res.*, doi:10.1016/j.jvolgeores.2017.01.020, in press.

Boore, D. M., and J. Boatwright (1984), Average body-wave radiation coefficients, *Bull. Seismol. Soc. Am.*, *74*, 1615–1621.

Bridges, D. L., and S. Gao (2006), Spatial variation of seismic b-values beneath Makushin Volcano, Unalaska Island, Alaska, *Earth Planet. Sci. Lett.*, *245*, 408–415.

Brune, J. (1970), Tectonic stress and the spectra of seismic shear waves from earthquakes, *J. Volcanol. Geotherm. Res.*, *75*, 4997–5009, doi:10.1029/JB075i026p04997.

Cañón Tapia, E. (2013), Analytical models of magma chamber stability: An abridged critical review of key concepts, *J. Volcanol. Geotherm. Res.*, *249*, 174–196, doi:10.1016/j.jvolgeores.2012.10.003.

Carbó, A., A. Muñoz-Martín, P. Llanes, J. Alvarez, and EEZ Working Group (2003), Gravity analysis offshore the Canary Islands from a systematic survey, *Mar. Geophys. Res.*, *24*, 113–127.

Carracedo, J. C., F. J. Pérez, E. Ancochea, J. Meco, F. Hernán, C. R. Cubas, R. Casillas, E. Rodriguez, and A. Ahijado (2002), Cenozoic volcanism II: The Canary Islands, in *The Geology of Spain*, pp. 439–472, edited by W. Gibbons and T. Moreno, Geol. Soc. of London, London, U. K.

Caudron, C., B. Taisne, Y. Kugaenko, and V. Saltykov (2015), Magma migration at the onset of the 2012–13 Tolbachik eruption revealed by Seismic Amplitude Ratio Analysis, *J. Volcanol. Geotherm. Res.*, *307*, 1 60–67, doi:10.1016/j.jvolgeores.2015.09.010.

Chiarabba, C., and M. Moretti (2006), An insight into the unrest phenomena at the CampiFlegrei caldera from Vp and Vp/Vs tomography, *Terra Nova*, *18*, 373–379, doi:10.1111/j.1365-3121.2006.00701.x

Chouet, B. A., and R. S. Matoza (2013), A multi-decadal view of seismic methods for detecting precursors of magma movement and eruption, *J. Volcanol. Geotherm. Res.*, *252*, 108–175, doi:10.1016/j.jvolgeores.2012.11.013.

Dach, R., S. Lutz, P. Walser, and P. Fridez (Eds.) (2015), *Bernese GNSS Software Version 5.2, User Manual*, Astron. Inst., Univ. of Bern, Bern Open Publ., Bern, doi:10.7892/boris.72297.

Dahm, T., S, Hainzl, and T, Fischer (2010), Bidirectional and unidirectional fracture growth during hydrofracturing: Role of driving stress gradients. *J. Geophys. Res.*, *115*, B12322, doi:10.1029/2009JB006817.

Del Fresno, C. (2016), Determinación de la Fuente Sísmica a Distancias Regionales: Aplicación a la serie de El Hierro 2011, PhD thesis, 228 pp., Univ. Complutense de Madrid, Madrid.

Del Fresno, C., I. Domínguez Cerdeña, E. Buforn, and C. López (2012), Source Time Function (STF) of the earthquake of the 8th October 2011 at El Hierro (Canary Islands), 7a Asamblea Hispano-Portuguesa de Geodesia y Geofísica, San Sebastian 2012, 820 pp.

Del Fresno, C., I. Domínguez Cerdeña, S. Cesca, and E. Buforn (2015), The 8 October 2011 Earthquake at El Hierro (Mw 4.0): Focal mechanisms of the mainshock and its foreshocks, *Bull. Seism. Soc. Am.*, *105*(1), 330–340, doi:10.1785/0120140151.

Díaz-Moreno, A., J. M. Ibáñez, S. DeAngelis, A. García-Yeguas, J. Prudencio, J. Morales, T. Tuvè, and L. García (2015), Seismic hydraulic fracture migration originated by successive deep magma pulses: The 2011–2013 seismic series associated to the volcanic activity of El Hierro Island, *J. Geophys Res. Solid Earth*, *120*, 7749–7770, doi:10.1002/2015JB012249.

Domínguez Cerdeña, I., C. del Fresno, and A. Gomis Moreno (2014), Seismicity patterns prior to the 2011 El Hierro Eruption, *Bull. Seismol. Soc. Am.*, *104*, 567–575, doi:10.1785/0120130200.

Dvorkin, J., G. Mavko, and A. Nur (1999), Overpressure detection from compressional-and shear-wave data, *Geophys. Res. Lett.*, *26*, 3417–3420.

Efron, B., and R. Tibshirani (1986), Bootstrap methods for standard errors, confidence intervals, and other measures of statistical accuracy, *Statist. Sci.*, *1*(1), 54–75, doi:10.1214/ss/1177013815. [Available at http://projecteuclid.org/euclid.ss/1177013815.]

Endo, E. T., and T. Murray (1991), Real-time seismic amplitude measurement (RSAM): A volcano monitoring tool, *Bull. Volcanol.*, *53*, 533–545.

Fischer, T., and A. Guest (2011), Shear and tensile earthquakes caused by fluid injection, *Geophys. Res. Lett.*, *38*, L05307, doi:10.1029/2010GL045447.

Frohlich, C., and K. D. Apperson (1992), Earthquake focal mechanisms, moment tensors, and the consistency of seismic activity near plate boundaries, *Tectonics*, *11*(2), 279–296, doi:10.1029/91TC02888.

García-Yeguas, A., J. M. Ibáñez, I. Koulakov, A. Jakovlev, M. C. Romero-Ruis, and J. Prudencia (2014), Seismic tomography model reveals mantle magma sources of recent volcanic activity at El Hierro Island (Canary Islands, Spain), *Geophys. J. Int.*, *199*(3), 1739–1750, doi:10.1093/gji/ggu339.

Geyer, A., J. Martí, and A. Villaseñor (2016), First-order estimate of the Canary Islands plate-scale stress field: Implications for volcanic hazard assessment, *Tectonophysics*, *679*, 125–139, doi:10.1016/j.tecto.2016.04.010.

González, P. J., S. V. Samsonov, S. Pepe, K. F. Tiampo, P. Tizzani, F. Casu, J. Fernández, A. G. Camacho, and E. Sansosti (2013), Magma storage and migration associated with the 2011–2012 El Hierro eruption: Implications for crustal magmatic systems at oceanic island volcanoes, *J. Geophys. Res. Solid Earth*, *118*, 4361–4377, doi:10.1002/jgrb.50289.

Gorbatikov, A. V., F. G. Montesinos, J. Arnoso, M. Y. Stepanova, M. Benavent, and A. A. Tsukanov (2013), New features in the subsurface structure model of El Hierro Island (Canaries) from low-frequency microseismic sounding: An insight into the 2011 seismo-volcanic crisis, *Surv. Geophys.*, *34*(4), 463–489, doi:10.1007/s10712-013-9240-4.

Green, R. G., T. Greenfield, and R. S. White (2015), Triggered earthquakes suppressed by an evolving stress shadow from a propagating dyke, *Nat. Geosci.*, *8*(8), 629–632, doi:10.1038/ngeo2491.

Gudmundsson, A. (2006), How local stresses control magma-chamber ruptures, dykeinjections, and eruptions in composite volcanoes, *Earth Sci. Rev.*, *79*(1–2), 1–31, doi:10.1016/j.earscirev.2006.06.006.

Gudmundsson, A. (2012), Magma chambers: Formation, local stresses, excess pressures, and compartments, *J. Volcanol. Geotherm. Res.*, *237–238*, 19–41, doi:10.1016/j.jvolgeores.2012.05.015.

Gutenberg, B., and C. F. Richter (1944), Frequency of the earthquakes in California, *Bull. Seismol. Soc. A*, *34*, 185–188.

Hanks, T. C., and H. Kanamori (1979), A moment magnitude scale, *J. Geophys. Res.*, *84*, 2348–2350, doi:10.1029/JB084iB05p02348.

Heimisson, E. R., P. Einarsson, F. Sigmundsson, and B. Brandsdottir (2015), Kilometer scale Kaiser-effect identified in Krafla volcano, Iceland, *Geophys. Res. Lett.*, *42*, 7958–7965, doi:10.1002/2015GL065680.

Hill, D. P., J. O. Langbein, and S. Prejean (2003), Relations between seismicity and deformation during unrest in Long Valley Caldera, California, from 1995 through 1999, *J. Volcanol. Geotherm. Res.*, *127*(2003) 175–193.

Hong, T. K., S. E. Houng, and E. Jo (2014), Temporal changes of medium properties during explosive volcanic eruption, *Geophys. Res. Lett.*, *41*, 1944–1950, doi:10.1002/2014GL059408.

Jackson, J., and D. McKenzie (1988), The relationship between plate motions and seismic moment tensors, and the rates of active deformation in the Mediterranean and Middle East, *Geophys. J. Int.*, *93*, 45–73.

Jo, E., and T. K. Hong (2013),VP/VS ratios in the upper crust of the southern Korean Peninsula and their correlations with seismic and geophysical properties, *J. Asian Earth Sci.*, *66*, 204–214.

Johnson, J. H., and M. P. Poland (2013), Seismic detection of increased degassing prior to Kīlauea's 2008 summit explosion, *Nat. Commun.*, *4*, Article 1668, doi:10.1038/ncomms2703.

Klügel, A., M.-A. Longpré, L. García-Cañada, and J. Stix (2015), Deep intrusions, lateral magma transport and related uplift at ocean island volcanoes, *Earth Planet. Sci. Lett.*, *431*, 140–149, doi:10.1016/j.epsl.2015.09.031.

Knopoff, L. (1971), Attenuation, in mantle and core, in *Planetary Physics*, edited by J. Coulomb, and M. Caputo, pp. 146–156, Elsevier, New York.

Kostrov, V. (1974), Seismic moment and energy of earthquakes, and seismic flow of rock, *Izv. Acad. Sci. USSR Phys. Solid Earth*, *1*, 23–44.

Koulakov, I., et al., (2012), Rapid changes in magma storage beneath the Klyuchevskoy group of volcanoes inferred from time-dependent seismic tomography, *J. Volcanol. Geotherm. Res.*, *263*, 75–91, doi:10.1016/j.jvolgeores.2012.10.014.

Larson, K. M., M. Poland, and A. Miklius (2010), Volcano monitoring using GPS: Developing data analysis strategies based on the June 2007 Kīlauea Volcano intrusion and eruption, *J. Geophys. Res.*, *115*, B07406, doi:10.1029/2009JB007022.

Lin, G., and P. M. Shearer (2009), Evidence for water-filled cracks in earthquake source regions, *Geophys. Res. Lett.*, *36*, L17315, doi:10.1029/2009GL039098.

Lin, J., and R. S. Stein (2004), Stress triggering in thrust and subduction earthquakes, and stress interaction between the southern San Andreas and nearby thrust and strike-slip faults, *J. Geophys. Res.*, *109*, B02303, doi:10.1029/2003JB002607.

Llanes, M. P. (2006), Estructura de la Litosfera en el Entorno de las Islas Canarias a partir del Análisis Gravimétrico e Isostático: Implicaciones Geodinámicas, doctoral thesis, pp. 1–189, Univ. Complutense de Madrid, Madrid.

Longpré, M. A., A. Klügel, A. Diehl, and J. Stix (2014), Mixing in mantle magma reservoirs prior to and during the 2011–2012 eruption at El Hierro, Canary Islands, *Geology*, *42*(4), 315–318.

López, C., et al. (2012), Monitoring the volcanic unrest of El Hierro (Canary Islands) before the onset of the 2011–2012 submarine eruption, *Geophys. Res. Lett.*, *39*, LI3303, doi:10.1029/2012GL051846.

López, C., J. Martí, R. Abella, and M. Tárraga (2014), Applying fractal dimensions and energy-budget analysis to characterize fracturing processes during magma migration and eruption: 2011–2012 El Hierro (Canary Islands) submarine eruption, *Surv. Geophys.*, *35*(4), 1023–1044, doi:10.1007/s10712-014-9290-2.

Maccaferri, F., M. Bonafede, and E. Rivalta (2011), A quantitative study of the mechanisms governing dike propagation, dyke arrest and sill formation, *J. Volcanol. Geotherm. Res.*, *208*, 39–50.

Martí, J., V. Pinel, C. López, A. Geyer, R. Abella, M. Tárraga, M. J. Blanco, A. Castro, and C. Rodríguez (2013), Causes and mechanisms of the 2011–2012 El Hierro (Canary Islands) submarine eruption, *J. Geophys. Res. Solid Earth*, *118*, 823–839, doi:10.1002/jgrb.50087.

Marti, J., C. López, S. Bartolini, L. Becerril, and A. Geyer (2016), Stress controls of monogenetic volcanism: A review, *Front. Earth Sci.*, *4*, Article 106, doi:10.3389/feart.2016.00106.

Martí, J., A. Villaseñor, A. Geyer, C. López, and A. Tryggvason (2017), Stress barriers controlling lateral migration of magma revealed by seismic tomography, *Sci. Rep.*, *7*, Article 40757, doi:10.1038/srep40757.

Masterlark, T. (2007), Magma intrusion and deformation predictions: Sensitivities to the Mogi assumptions, *J. Geophys. Res.*, *112*, B06419, doi:10.1029/2006JB004860.

Maxwell, S. C., C. K. Waltman, N. R. Warpinski, M. J. Mayerhofer, and N. Boroumand (2006), Imaging seismic deformation induced by hydraulic fracture complexity, *SPE Pap. 102801*, Proceedings, Society of Petroleum Engineers Annual Technical Conference.

McNutt, S. (2005), Volcanic seismology, *Annu. Rev. Earth Planet. Sci.*, *32*, 461–491.

McTigue, D. F. (1987), Elastic stress and deformation near a finite spherical magma body—Resolution of the point-source paradox, *J. Geophys. Res.*, *92*, 12,931–12,940.

Meletlidis, S., A. Di Roberto, I. Domínguez Cerdeña, M. Pompilio, L. García-Cañada, A. Bertagnini, M. A. Benito-Saz, P. Del Carlo, and S. Sainz-MazaAparicio (2015), New insight into the 2011–2012 unrest and eruption of El Hierro Island (Canary Islands) based on integrated geophysical, geodetical and petrological data, *Ann. Geophys.*, *58*(5), S0546-1–S0546-20, doi:10.4401/ag-6754.

Miller, S. A., C. Collettini, L. Chiaraluce, M. Cocco, M. R. Barchi, and B. Kaus (2004), Aftershocks driven by a high pressure CO_2 source at depth, *Nature*, *427*, 724–727.

Montesinos, F. G., J. Arnoso, M. Benavent, and R. Vieira (2006), The crustal structure of El Hierro (Canary Islands) from 3-D gravity inversion, *J. Volcanol. Geotherm. Res.*, *150* (1–3), 283–299, doi:10.1016/j.jvolgeores.2005.07.018.

Murru, M., R. Console, G. Falcone, C. Montuori, and T. Sgroi (2007), Spatial mapping of the b-value at Mount Etna, Italy, using earthquake data recorded from 1999 to 2005, *J. Geophys. Res.*, *112*, B12303, doi:10.1029/2006JB004791.

Núñez, A. (2017), Simulación de escenarios sísmicos mediante un Sistema de Información Geográfica para la Península Ibérica, las Islas Baleares y las Islas Canarias, considerando el efecto de sitio y las dimensiones y características de la fuente sísmica, doctoral thesis, 455 pp., Univ. Politécnica de Madrid, Madrid.

Okada, Y. (1992), Internal deformation due to shear and tensile faults in a half-space, *Bull. Seismol. Soc. Am.*, *82*(2), 1018–1040.

Patanè, D., G. Barberi, O. Cocina, P. De Gori, and C. Chiarabba (2006), Time resolved seismic tomography detects magma intrusions at Mount Etna, *Science*, *313*, 821–823, doi:10.1126/science.1127724.

Phillipson, G., R. Sobradelo, and J. Gottsmann (2013), Global volcanic unrest in the 21st century: An analysis of the first decade, *J. Volcanol. Geotherm. Res.*, *264*, 183–196, doi:10.1016/j.jvolgeores.2013.08.004.

Pinel, V., and C. Jaupart (2004), Magma storage and horizontal dyke injection beneath a volcanic edifice, *Earth Planet Sci. Lett.*, *221*, 245–262.

Roman, D. C., and P. Heron (2007), Effect of regional tectonic setting on local fault response to episodes of volcanic activity, *Geophys. Res. Lett.*, *34*, L13310, doi:10.1029/2007GL030222.

Roman, D. C., M. Rodgers, H. Geirsson, P. C. LaFemina, and V. Tenorio (2016), Assessing the likelihood and magnitude of volcanic explosions based on seismic quiescence, *Earth Planet. Sci. Lett.*, *450*, 20–28, doi:10.1016/j.epsl.2016.06.020.

Sainz-Maza, S., J. Arnoso, F. G. Montesinos, and J. Martí (2014), Volcanic signatures in time gravity variations during the volcanic unrest on El Hierro (Canary Islands), *J. Geophys. Res. Solid Earth*, *119*, 5033–5051, doi:10.1002/2013JB010795.

Shapiro, S. A., E. Huenges, and G. Borm (1997), Estimating the crust permeability from fluid-injection-induced seismic emission at the KTB site, *Geophys. J. Int.*, *131*, F15–F18, doi:10.1111/j.1365-246X.1997.tb01215.x.

Shapiro, S. A., O. S. Krueger, C. Dinske, and C. Langenbruch (2011), Magnitudes of induced earthquakes and geometric scales of fluid stimulated rock volumes, *Geophysics*, *76*, WC55–WC63.

Sigmundsson, F., et al. (2015), Segmented lateral dyke growth in a rifting event at Bardarbunga volcanic system, Iceland, *Nature*, *517*(7533), 191–195

Sparks, R, (2003), Forecasting volcanic eruptions, *Earth Planet. Lett.*, *2010*(1–2), 1–15, doi:10.1016/S0012821X(03)001249.

Stich, D., E. Serpelloni, F. Mancilla, and J. Morales (2006), Kinematics of the Iberia–Maghreb plate contact from seismic moment tensors and GPS observations, *Tectonophysics*, *426*(3–4), 295–317, doi:10.1016/j.tecto.2006.08.004.

Stroncik, N. A., A. Klügel, and T. H. Hansteen (2009), The magmatic plumbing system beneath El Hierro (Canary Islands): Constraints from phenocrysts and naturally quenched basaltic glasses in submarine rocks, *Contrib. Mineral. Petrol.*, *157*, 593–607, doi:10.1007/s00410-008-0354-5.

Tárraga, M., J. Martí, R. Abella, R. Carniel, and C. López (2014), Volcanic tremors: Good indicators of change in plumbing systems during volcanic eruptions, *J. Volcanol. Geotherm. Res.*, *273*, 33–40.

Telesca, L., M. Lovallo, J. Martì, C. López, and R. Abella (2014), Using the Fisher-Shannon method to characterize continuous seismic signal during volcanic eruptions: Application to 2011–2012 El Hierro (Canary Islands) eruption, *Terra Nova*, *26*, 425–429, doi:10.1111/ter.12114.

Telesca, L., M. Lovallo, J. Martì, C. López, and R. Abella (2015), Multifractal investigation of continuous seismic signal recorded at El Hierro volcano (Canary Islands) during the 2011–2012 pre- and eruptive phases, *Tectonophysics*, *642*, 71–77, doi:10.1016/j.tecto.2014.12.019.

Toda, S., R. Stein, and T. Sagiya (2002), Evidence from the AD 2000 Izu islands earthquake swarm that stressing rate governs seismicity, *Nature*, *419*, 58–61.

Toda, S., R. S. Stein, K. Richards-Dinger, and S. Bozkurt (2005), Forecasting the evolution of seismicity in southern California: Animations built on earthquake stress transfer, *J. Geophys. Res.*, *110*, B05S16, doi:10.1029/2004JB003415.

Traversa, P., V. Pinel, and J. A. Grasso (2010), Constant influx model for dike propagation: Implications for magma reservoir dynamics, *J. Geophys. Res.*, *115*, B01201, doi:10.1029/2009JB006559.

Tregoning, P., and T. A. Herring (2006), Impact of a priori zenith hydrostatic delay errors on GPS estimates of station heights and zenith total delays, *Geophys. Res. Lett.*, *33*, L23303, doi:10.1029/2006GL027706.

Unglert, K., M. K. Savage, N. Fournier, T. Ohkura, and Y. Abe (2011), Shear wave splitting, VP/VS, and GPS during a time of enhanced activity at Aso caldera, Kyushu, *J. Geophys. Res.*, *116*, B11203, doi:10.1029/2011JB008520.

Vinciguerra, S. (2002), Damage mechanics preceding the September-October 1989 flank eruption at Mount Etna volcano inferred by seismic scaling exponents, *J. Volcanol. Geotherm. Res.*, *113*, 391–397.

Wadati, K. (1933), On the travel time of earthquake waves, II, *Geophys. Mag.*, *7*, 101–111.

Walter, T. R., and F. Amelung (2007), Volcanic eruptions following M$\geq$9 megathrust earthquakes: Implications for the Sumatra-Andaman volcanoes, *Geology*, *35*, 539–542, doi:10.1130/G23429A.1.

Wassermann, J. (2012), Volcano seismology, in *New Manual of Seismological Observatory Practice 2 (NMSOP-2)*, edited by P. Bormann, GFZ German Res. Cent. for Geosci., Potsdam.

Watts, A. B. (1994), Crustal structure, gravity-anomalies and flexure of the lithosphere in the vicinity of the Canary-Islands, *Geophys. J. Int.*, *119*(2), 648–666, doi:10.1111/j.1365-246X.1994.tb00147.x.

Watts A. B., C. Peirce, J. Collie, R. Dalwood, J. P. Canales, and T. J. Henstock (1997), A seismic study of lithospheric flexure at Tenerife, Canary Islands, *Earth Planet. Sci. Lett.*, *146*, 431–448.

Wiemer, S. (2001), A software package to analyze seismicity: ZMAP, *Seismol. Res. Lett.*, *72*, 373–382.

Wiemer, S., and M. Wyss (2002), Mapping spatial variability of the frequency-magnitude distribution of earthquakes, *Adv. Geophys.*, *45*, 259–302.

Zang, A., and O. Stephansson (2010), *Stress Field of the Earth's Crust*, Springer, Dordrecht, Netherlands.